

# Tuning the Magnetization of Manganese (II) Carbonate by Intracrystalline Amino Acids

Arad Lang, Iryna Polishchuk, Giorgia Confalonieri, Catherine Dejoie, Ariel Maniv, Daniel Potashnikov, El'ad N. Caspi, and Boaz Pokroy\*

Incorporation of organic molecules into the lattice of inorganic crystalline hosts is a common phenomenon in biomineralization and is shown to alter various properties of the crystalline host. Taking this phenomenon as a source of inspiration, it is shown herein that incorporation of specific single amino acids into the lattice of manganese (II) carbonate strongly alters its inherent magnetic properties. At room temperature, the magnetic susceptibility of the amino-acid-incorporating paramagnetic  $\text{MnCO}_3$  decreases, following a simple rule of mixtures. When cooled below the Néel temperature, however, the opposite trend is observed, namely an increase in magnetic susceptibility measured in a high magnetic field. Such an increase, accompanied by a drastic change in the Néel phase transformation temperature, results from a decrease in  $\text{MnCO}_3$  orbital overlapping and the weakening of superexchange interactions. It may be that this is the first time that the magnetic properties of a host crystal are tuned via the incorporation of amino acids.

## 1. Introduction

Inorganic crystals grown by organisms via biomineralization processes demonstrate fascinating strategies of crystal growth.<sup>[1]</sup> Their structures, from the atomic to the micrometer scale, are tailored to serve specific functions such as mechanical (mastication,<sup>[2,3]</sup> shielding,<sup>[4,5]</sup> and support,<sup>[6,7]</sup>), optical<sup>[8]</sup> and magnetic.<sup>[9–13]</sup> A widespread strategy of biogenic crystal growth is the incorporation of organic molecules into the lattice of an inorganic crystalline host,<sup>[14–16]</sup> a procedure that has been also shown to induce lattice distortions in the host biocrystals.<sup>[17]</sup> Such incorporation is one of the main reasons for the superior mechanical properties of biominerals.<sup>[18,19]</sup> This biostrategy has been translated, for example, to synthetic calcium carbonate ( $\text{CaCO}_3$ ) which is shown to incorporate

block copolymers,<sup>[20]</sup> polymeric micelles,<sup>[21,22]</sup> hydrogels,<sup>[23–25]</sup> dyes,<sup>[26]</sup> drugs,<sup>[27]</sup> peptides,<sup>[15,28,29]</sup> and monosaccharaides,<sup>[30]</sup> as well as single amino acids (AAs).<sup>[31–33]</sup> In each of these cases, the unit cell dimensions of the resulting composite calcite crystals were altered, as the lattice parameters were elongated,<sup>[33]</sup> shortened,<sup>[29]</sup> or a combination of the two.<sup>[30]</sup> In the case of AAs incorporation, similar to biominerals, the hardness of the calcitic host increases with the increase of organic content.<sup>[32]</sup>

Various single AAs have also been incorporated into a variety of synthetic semiconductors, including zinc oxide ( $\text{ZnO}$ ),<sup>[34,35]</sup> copper oxide ( $\text{Cu}_2\text{O}$ ),<sup>[36]</sup> and methylammonium lead bromide ( $\text{MAPbBr}_3$ ).<sup>[37]</sup> Such incorporation not only induces lattice distortions but also increases the optical band gap of the crystalline host, as was measured based on the reflectance ( $R$ ) and the photoluminescence (PL) spectra of the studied samples. The blueshift originates from the insulating nature of the AAs, which act as a potential barrier inside the semiconducting matrix and induce a quantum confinement effect.<sup>[38]</sup>

In this study, we aimed to determine whether incorporation of AAs into a magnetic crystalline host influences its magnetic properties. To this end, we chose to study the magnetic properties of manganese (II) carbonate ( $\text{MnCO}_3$ , rhodochrosite, henceforth MCO). MCO was chosen as it possesses the same crystal structure and synthesis route as those of the well-studied calcite ( $R\bar{3}c$  space group).<sup>[39]</sup> MCO is paramagnetic (PM) at room temperature and undergoes transformation to its antiferromagnetic (AFM) phase at a Néel temperature of

A. Lang, I. Polishchuk, B. Pokroy  
Department of Materials Science and Engineering and The Russell  
Berrie Nanotechnology Institute  
Technion – Israel Institute of Technology  
Haifa 32000, Israel  
E-mail: bpokroy@technion.ac.il

G. Confalonieri, C. Dejoie  
ESRF - The European Synchrotron Radiation Facility  
CS 40220, Grenoble, Cedex 9 38043, France

A. Maniv, E. N. Caspi  
Physics Department  
Nuclear Research Centre - Negev  
P.O. Box 9001, Beer-Sheva 84190, Israel

D. Potashnikov  
Israel Atomic Energy Commission  
P.O. Box 7061, Tel-Aviv 61070, Israel

B. Pokroy  
The Nancy and Stephen Grand Technion Energy Program  
Technion – Israel Institute of Technology  
Haifa 3200003, Israel

 The ORCID identification number(s) for the author(s) of this article can be found under <https://doi.org/10.1002/adma.202201652>.

© 2022 The Authors. Advanced Materials published by Wiley-VCH GmbH. This is an open access article under the terms of the Creative Commons Attribution-NonCommercial-NoDerivs License, which permits use and distribution in any medium, provided the original work is properly cited, the use is non-commercial and no modifications or adaptations are made.

DOI: 10.1002/adma.202201652

$T_N \approx 32$  K.<sup>[40]</sup> It belongs to a family of materials, which, while in their AFM phase, exhibit weak ferromagnetism (WFM). The latter is owing to spin canting, in which the spin vectors of the Mn atoms are tilted out of the *ab* plane of the crystal, resulting in a weak ferromagnetic response (also known as the Dzyaloshinskii–Moriya interaction, DMI).<sup>[41–44]</sup> MCO can be utilized in a variety of applications, including supercapacitors,<sup>[45–47]</sup> lithium-ion battery anodes,<sup>[48–50]</sup> plant fertilizers,<sup>[51]</sup> light emitters,<sup>[52]</sup> hematinic agents,<sup>[53]</sup> and contrast enhancing agents for magnetic resonance imaging (MRI).<sup>[54,55]</sup>

## 2. Results

MCO was synthesized via both room-temperature drop-by-drop (DD) and hydrothermal (HT) methods, in the presence of the identical molar concentration ( $80 \times 10^{-3}$  M) in solution of four common L-form amino acids (L-AAs): aspartic acid (Asp), glutamic acid (Glu), glycine (Gly), and cysteine (Cys). These AAs were selected because they are the ones with the most significant levels of incorporation into calcite (for more details, see Experimental Section).<sup>[31,33,56]</sup> Cys was used only in the DD method, in order to avoid its decomposition at elevated temperatures. **Figure 1** presents the change in magnetic susceptibility of AA-incorporating MCO compared to that of pure MCO

(see magnetic moment versus magnetic field plots (*M–H*) presented in Figure S1, Supporting Information). The magnetic susceptibility ( $\chi$ ) was calculated as the slope of the linear part of the normalized measured magnetization (*m*) in relation to the external magnetic field (*H*), that is:

$$\chi \equiv \frac{\partial m}{\partial H} [\text{emu Oe}^{-1} \text{ gr}^{-1}] \quad (1)$$

Figure 1 shows, interestingly, that the magnetic susceptibility of MCO was indeed altered owing to the incorporation of AAs. This alteration was more pronounced in the HT-grown samples than in the DD-grown ones, even though the AA concentration in solution was identical in both cases. This clear observation provided an indication of intracrystalline AA incorporation, as the incorporation level in the crystals grown via HT synthesis was also higher in the case of calcite.<sup>[33]</sup> Even more striking were the opposite effects of AAs incorporation at the two different temperatures: while the change in magnetic susceptibility due to incorporation decreased at room temperature, it increased dramatically at 2 K. An exception was observed in the case of Cys-incorporating MCO, whose magnetic susceptibility at both temperatures decreased.

As both Asp and Cys showed the strongest effects on the magnetic susceptibility of MCO (Figure 1), we further proceeded to study the effects of various concentrations of these two AAs. To this end, we added Asp or Cys into the solution at the concentrations of 20, 50, and  $80 \times 10^{-3}$  M. The exact amount of the incorporated AA was determined by amino acid analysis (AAA). The amount of incorporated AA was found to increase with its increasing concentration in the growth solution, reaching the highest level of  $\approx 8$  mol% in the case of Asp (Figure S2, Supporting Information). Interestingly, the incorporation level of Asp within the MCO lattice was of the same order of magnitude as that observed in the case of calcite,<sup>[33]</sup> and as expected, the incorporation levels achieved via HT growth due to higher temperature and pressure were higher than those achieved via the DD method.

We employed synchrotron high-resolution powder X-ray diffraction (HR-PXRD) to detect changes in MCO structure and microstructure caused by the incorporation of Asp. **Figure 2a** depicts representative interplanar spacings of the (104) plane, which is the most intense reflection of MCO (Figure S3, Supporting Information), for both the pure and the Asp-incorporating MCO. The *d*-spacings of the Asp-incorporating sample were larger than those of the control sample. Such relative expansion is a known fingerprint for the incorporation of organic molecules.<sup>[31,34,57]</sup> Moreover, following a mild thermal annealing (200 °C for 4 h, in vacuum), which induces decomposition of the incorporated organics, the diffraction peaks shifted to smaller *d*-values. This is also a fingerprint, this time for incorporation of the organics within the crystalline lattice.<sup>[31,34]</sup> Furthermore, Figure 2a clearly demonstrates a significant broadening of the diffraction peaks upon Asp incorporation, suggesting a decrease in the crystallite size of the material. This suggestion is further supported by the high-resolution scanning electron microscopy (HR-SEM) images of the crystals (Figure S4, Supporting Information). Additional evidence for lattice incorporation can be derived from the evolution of the

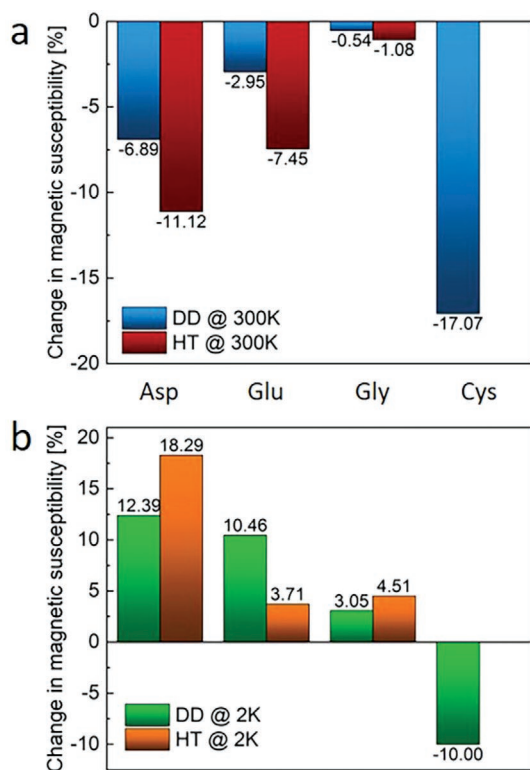


**Figure 1.** Changes in magnetic susceptibility of AA-incorporating MCO. a,b) Changes in the magnetic susceptibilities of MCO grown via HT and DD methods, in the presence of the same concentration ( $80 \times 10^{-3}$  M) of selected L-AAs, measured at 300 K (a) and 2 K (b). Changes were calculated relative to pure MCO. The maximum relative error is 0.05% of the presented values.

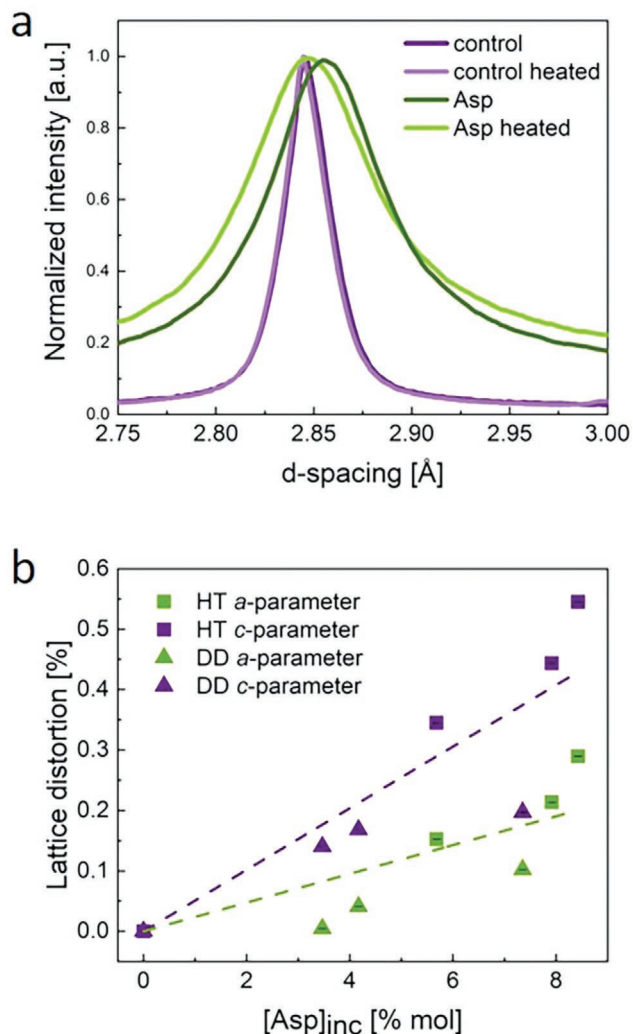


**Figure 2.** Lattice distortions in Asp-incorporating MCO. a) The (104) reflection of both pure and Asp-incorporating MCO, before and after thermal annealing. b) Lattice distortions in *a*- and *c*-parameters of MCO as a function of the amount of the incorporated Asp. The error bars are smaller than the data points.

coherence length upon annealing, calculated via the Lorentzian contribution to the broadening full width half maximum (FWHM) of the diffraction peaks (Figure S5, Supporting Information).<sup>[58]</sup> Although after a mild heat treatment, the coherence length of the control samples was slightly increased (because of crystal growth due to annealing), it decreased in the case of Asp-incorporating crystals. This decrease was due to the creation of new defects upon organic degradation.<sup>[58]</sup> In the case of Cys, HR-PXRD revealed the formation of an additional phase ( $\alpha$ -Mn<sub>2</sub>O<sub>3</sub>, bixbyite), whose amount increased with the increase in incorporated Cys in the crystal (Figure S11, Supporting Information). The decrease in magnetic susceptibility of Cys-incorporating MCO, observed both at 300 and 2 K (Figure 1; Figure S11d, Supporting Information), stems from the formation of this second phase (for more details, see Supporting Information).

We used Rietveld refinement to accurately extract the lattice parameters (both *a* and *c*) of each sample, and calculated the lattice distortion according to the equation:

$$\frac{\Delta a}{a} = \frac{a_A - a_C}{a_C}; \quad \frac{\Delta c}{c} = \frac{c_A - c_C}{c_C} \quad (2)$$

where *a*<sub>A</sub> and *c*<sub>A</sub> are the lattice parameters of the Asp-incorporating samples and *a*<sub>C</sub> and *c*<sub>C</sub> are those of the control sample. Similar to the case of calcite,<sup>[31]</sup> the MCO distortion was positive and anisotropic, and its magnitude increased with the amount of incorporated Asp (as measured here by AAA). In particular, when comparing the lattice distortions induced by similar amounts of Asp in MCO and in calcite grown via the HT method, one can find that the measured distortion of the *c* lattice parameter is similar to that of calcite.<sup>[33]</sup> In addition, and akin to calcite,<sup>[33]</sup> the HT method allowed the incorporation of higher AAs levels into the MCO lattice, where higher incorporated concentration leads to higher lattice distortions (Figure 2).

To further study the effects of AAs incorporation on the crystal structure and on the magnetic structure of MCO, we employed neutron powder diffraction (NPD). The structural parameters obtained via NPD were in good agreement with those obtained by HR-PXRD (Figure S6a, Supporting Information). More specifically, NPD also confirmed the presence of anisotropic lattice distortions (in which the distortions along the *c* lattice parameter were greater than those along the *a* lattice parameter), as well as broadening of the diffraction peaks due to Asp incorporation (Figure S6c, Supporting Information). One distinct feature observed by NPD was the dramatic increase in background intensity for the Asp-incorporating samples compared to that of the control. This is probably due to the hydrogen atoms present in Asp, which are known to increase the background intensity in NPD patterns.<sup>[59]</sup>

Following the above structural analysis, magnetization of the MCO samples was measured utilizing an MPMS3 SQUID magnetometer (Quantum Design). Figure 3a,c depicts the magnetization of both pure and Asp-incorporating HT-grown MCO as a function of the applied magnetic field (between −1 and 1 T). The *M*–*H* plots measured at room temperature (Figure 3a) were characteristic of a PM phase while those measured at 2 K fit a canted AFM phase<sup>[60,61]</sup> (Figure 3c). Similar results were obtained for the DD-grown samples (for the complete curves, see Figure S7, Supporting Information). Both the extent of decrease in magnetic susceptibility at room temperature and its increase at 2 K were found to be dependent on the concentration of incorporated Asp (Figure 3b,d). Note, that the samples demonstrated the same trend at the higher magnetic field between −7 and 7 T as that between −1 and 1 T (Figure S8, Supporting Information).

Interestingly, along with the induced changes in magnetic susceptibility, Asp incorporation significantly affected the Néel temperature (*T*<sub>N</sub>) of MCO, namely the temperature of magnetic phase transformation (Figure 3e,f). A decrease of over 20% in *T*<sub>N</sub> (by ≈6 K) was achieved at the maximum concentration of incorporated Asp (≈8 mol%). Similar to the changes in  $\chi$  upon Asp incorporation, the extent of change in *T*<sub>N</sub> was dependent on the amount of incorporated Asp rather than on the method of synthesis.

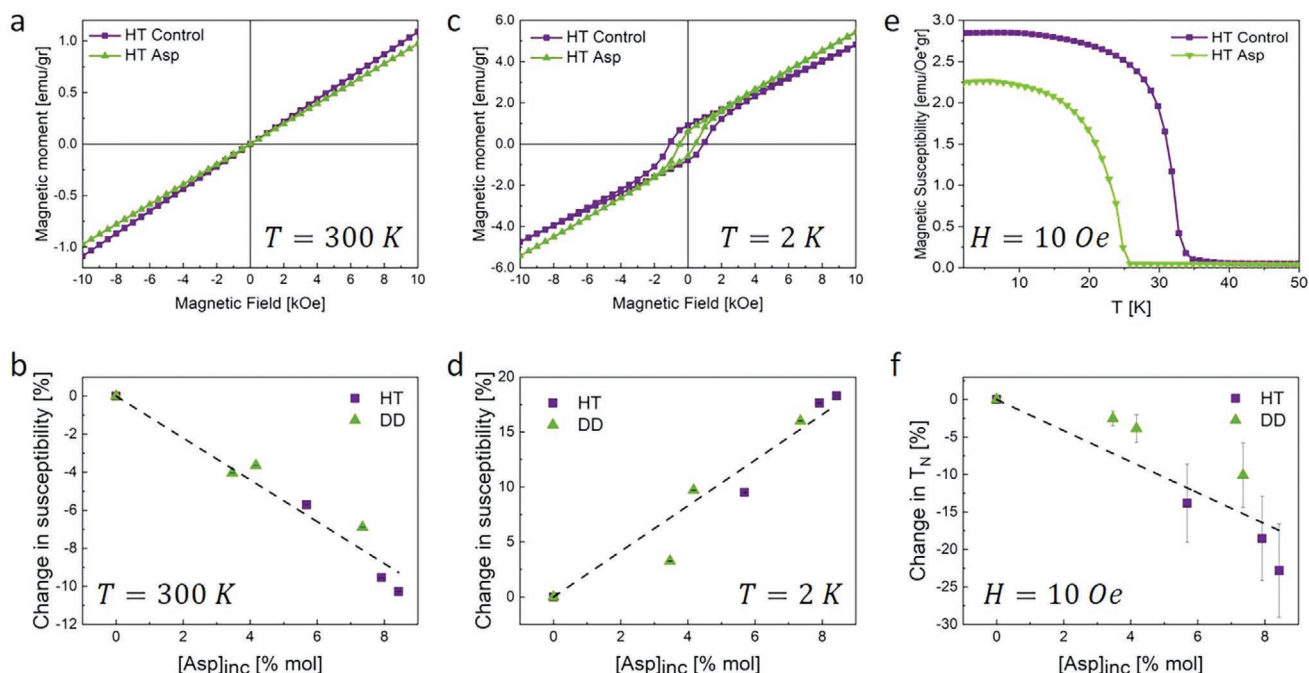


**Figure 3.** Changes in magnetic properties of MCO due to incorporation of Asp. a,b) Decrease in magnetic susceptibility measured at room temperature. c,d) Increase in magnetic susceptibility measured at 2 K. e,f) Decrease in  $T_N$  measured during heating at zero magnetic field relative to the control sample. In (b,d), the error bars are smaller than the data points.

To further study the effects of Asp incorporation on the magnetic properties of MCO, we repeated our NPD measurements below  $T_N$ , at a temperature of 3 K. Additional diffraction peaks were observed due to the magnetic phase transformation (Figure S7b,d, Supporting Information). The quality of these NPD data did not allow for determination of the WFM known to exist in MCO<sup>[43,44]</sup> and also observed in this study (Figure 3c). However, the AFM portion of the magnetic ordering was easily determined using Rietveld refinement when we used a model exhibiting  $C2'/c'$  symmetry (#15.89)<sup>[62]</sup> (Figure 4). We first

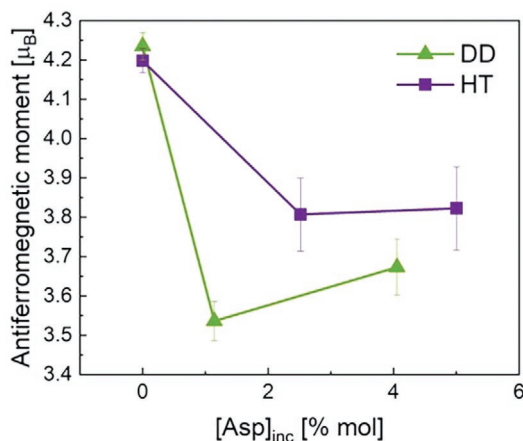


**Figure 4.** Changes in antiferromagnetic moment of MCO. Ordered AFM moment of MCO is determined via Rietveld refinement utilizing the magnetic symmetry model  $C2'/c'$  (#15.89) in the basis (a,b,c)(0,0,0) of the parent space group  $R\bar{3}c$  to the NPD data.

extracted the magnetic moments for both of the control samples derived via the synthesis routes DD and HT and found that these magnetic moment values were in an excellent agreement with known published data ( $\approx 4.2 \mu_B$ ).<sup>[44]</sup> Similar extractions in the case of the Asp-incorporating samples, however, resulted in significant reductions in the ordered magnetic moments.

### 3. Discussion

At room temperature, the magnetic susceptibility of MCO decreased with increasing Asp concentration (Figure 3a–c). This was probably due to the formation of a composite material. To verify this assumption, we measured the susceptibility of a pure Asp powder (Figure S10, Supporting Information) and used the rule of mixtures to calculate the expected susceptibility of the composite:

$$\chi_{\text{total}} = w_{\text{Asp}} \chi_{\text{Asp}} + (1 - w_{\text{Asp}}) \chi_{\text{MCO}} \quad (3)$$

where  $w_{\text{Asp}}$  is the weight fraction of incorporated Asp (as obtained by AAA) and  $\chi_{\text{Asp}}$  and  $\chi_{\text{MCO}}$  are the susceptibilities of pure Asp and pure MCO (control samples), respectively. Figure 5a indeed demonstrates a good correlation between the measured data and the calculated prediction.

In contrast to PM susceptibility at room temperature, the increase in MCO susceptibility measured at  $T = 2$  K cannot be explained by a simple rule of mixtures. To explain this effect, we first need to understand what types of magnetic interaction exists in MCO. At low temperatures (below the  $T_N$ ), MCO is an asymmetric superexchange magnet (i.e., it demonstrates

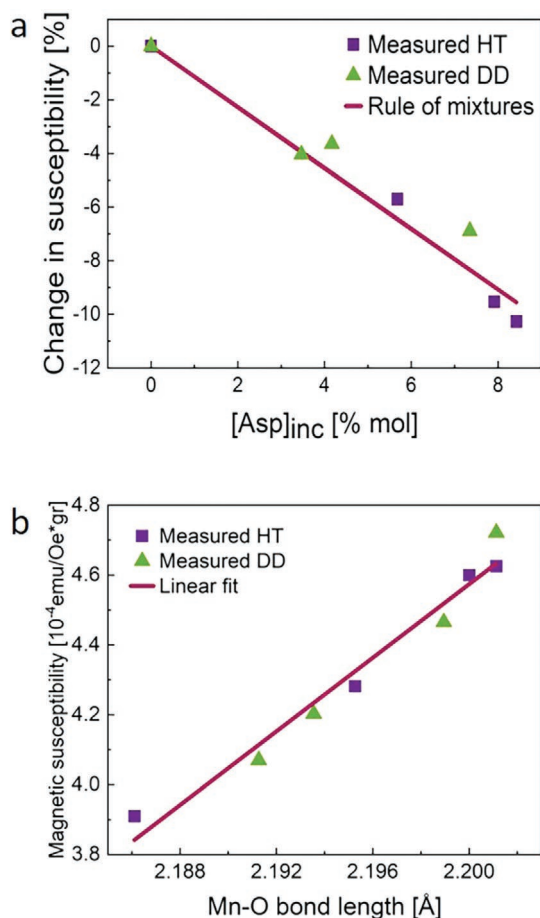


**Figure 5.** Suggestions for the observed changes in magnetic susceptibilities. a) Decrease at room temperature: comparison between the measured susceptibilities and the calculated prediction using Equation (3). b) Increase at low temperature: measured susceptibilities as a function of the Mn–O distance in the crystal. Error bars are smaller than data points.

the so-called Dzyaloshinskii–Moriya interaction, DMI).<sup>[43,44]</sup> According to this model, the spin vectors of the magnetic cations interact via bridging of the non-magnetic anions<sup>[63]</sup>—an interaction known to be strongly dependent on their interatomic distance.<sup>[64]</sup> In the case of the low-temperature MCO, the AFM ordering of the Mn<sup>2+</sup> cations occurs due to interaction through the oxygen atoms, while the alternating orientation of the CO<sub>3</sub><sup>2-</sup> anions induces an out-of-plane spin canting, which leads to the observed WFM.<sup>[43,44,60]</sup> Probably, the positive lattice distortion (Figure 2b) induced by the Asp incorporation weakens the DMI by increasing the Mn–O distance. Hence, the crystal becomes more “magnetically compliant”, that is, its low-temperature susceptibility increases and the WFM hysteresis loop narrows more rapidly (Figure 3c). Moreover, this reduced interaction allows the magnetic ordering to break at lower temperatures, resulting in a decrease of the  $T_N$  (Figure 3e,f). To verify this hypothesis, we used cryo-HR-PXRD to measure the lattice parameters of MCO at 5 K. Figure 5b presents the magnetic susceptibility (taken at the linear region of the  $M-H$  plot measured at 2 K) as a function of the Mn–O interatomic distance calculated using the previously reported equations

developed for isostructural calcite<sup>[65]</sup> (see full HR-PXRD pattern in Figure S11 and Table S3, Supporting Information). The existing strong correlation ( $R^2 = 0.96$ ) indeed suggested that the increase in bond length, which reduces the Mn–3d and O–2p orbitals overlap, reduces the magnetic superexchange interaction in the crystals, thus resulting in a higher susceptibility and a narrower magnetic hysteresis loop.

The significant reduction in the ordered magnetic moment of MCO as a function of Asp incorporation, as observed by NPD, cannot be easily explained in terms of weakening of the DMI. Such a reduction might be correlated to a possible change in lattice symmetry driven by this incorporation. If such a change in symmetry indeed exists, we could hypothesize that the chosen refinement model is not ideal and that a reduction in symmetry should be considered and sought. An additional indication of such a symmetry reduction on the crystallographic level can be demonstrated by refining the oxygen positions of the  $C2'/c'$  space group (Figure 6). When these atomic positions were refined to fit the diffraction data of the DD sample

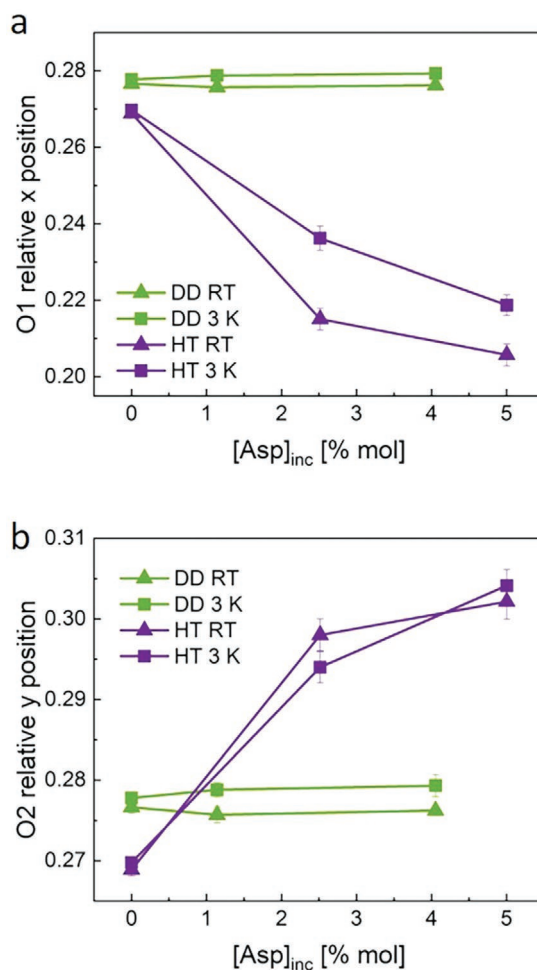


**Figure 6.** Changes in the relative oxygen position due to Asp incorporation. Relative oxygen position as a function of Asp concentration, as determined by application of Rietveld refinement to the NPD data by using the  $C2'/c'$  magnetic space group in the (a,b,c) (0,0,0) basis of the parent  $R\bar{3}c$  space group. In this model: a) O1 is positioned in ( $x \approx 0.25$ , 0,  $\frac{1}{4}$ ) and b) O2 is positioned in (0,  $y = 0.25$ ,  $\frac{1}{4}$ ).

or of the control, identical atomic positions emerged for both O1 and O2. Moreover, this position value ( $\approx 0.28$ ) was the value expected when the parent  $R\bar{3}c$  symmetry was used to refine the data. In practice, therefore, no reduction in crystallographic symmetry was expected for these samples. However, when the same refinement process was repeated for the HT samples collected at both RT and 3 K, a clear split was observed between the O1 and the O2 positions. This splitting became more prominent upon incorporation of higher amounts of Asp (Figure 6). These results clearly suggested that incorporation of Asp under the HT process, which is known to lead to higher incorporation levels of AAs, caused a reduction in the crystallographic symmetry.

#### 4. Conclusion

We have shown for the first time that incorporation of AAs into the crystal lattice of manganese (II) carbonate induces significant changes in its magnetic susceptibility. This phenomenon depends on the magnetic ordering of MCO. At room temperature, MCO is inherently paramagnetic and its susceptibility upon incorporation of AAs decreases following the simple rule of mixture. At low temperatures, MCO is a canted antiferromagnet, which exhibits weak ferromagnetism. Upon AA incorporation, it becomes more magnetically compliant owing to weakening of the superexchange interaction, induced by AAs-incorporation-governed lattice expansion. Moreover, as a result of the AAs incorporation, the transformation temperature of these two magnetic states is decreased.

This study demonstrates the feasibility of tuning the magnetic properties of a crystalline host via a bioinspired route, namely incorporation of AAs. This method facilitates the use of small, organic biomolecules, which provide the control over the magnetic properties of the host, without the need of changing its chemical structure or stoichiometry. Given the tunability of magnetic properties demonstrated here is based on the change in interatomic distances, we strongly believe that this method can be applied to other magnetic crystals possessing superexchange interactions (among them are  $\text{Fe}_3\text{O}_4$ ,<sup>[66]</sup>  $\text{CuO}$ ,<sup>[67]</sup> and  $\text{CrO}_2$ <sup>[68]</sup>). Moreover, we believe that the concept described in this study can be expanded to incorporation of other organic and inorganic species (for example, monosaccharides<sup>[30]</sup> and silica nanoparticles<sup>[69]</sup>). However, as the magnetic interaction gets complicated due to incorporation of magnetically-interacting species, such as metallic<sup>[70]</sup> or even magnetic<sup>[24]</sup> nanoparticles, it becomes more difficult to predict the overall magnetic outcome. Overall, this method opens a new avenue of research in the realm of magnetic materials and paves the way to a novel approach to the tailoring of their magnetic properties.

#### 5. Experimental Section

**Materials:** Stock solutions of 0.2 M  $\text{Mn}^{2+}$  and  $\text{CO}_3^{2-}$  were prepared by dissolving, respectively, 19.79 g of manganese chloride tetrahydrate ( $\text{MnCl}_2 \times 4\text{H}_2\text{O}$ , Fisher Scientific) and 10.60 g of sodium carbonate ( $\text{Na}_2\text{CO}_3$ , Mercury) in 500 mL of DI  $\text{H}_2\text{O}$ . Different amounts of L-aspartic acid (Asp, Sigma-Aldrich), L-glutamic acid (Gly, Alfa Aesar), L-glycine (Gly, Sigma-Aldrich), and L-cysteine (Cys, Sigma-Aldrich) were used.

**$\text{MnCO}_3$  Synthesis:** Synthesis was carried out via two routes: i) room temperature drop-by-drop (DD) method:<sup>[31]</sup> following transfer of 50 mL of  $\text{CO}_3^{2-}$  solution to a glass beaker, an appropriate amount of an L-AA was added to the solution (20, 50, and  $80 \times 10^{-3}$  M of Asp or Cys,  $80 \times 10^{-3}$  M of Gly or Glu), and stirring was continued until the AA was completely dissolved. Meanwhile, 50 mL of  $\text{Mn}^{2+}$  solution was loaded into a plastic syringe, which was placed in a syringe pump. MCO precipitation was initiated by the slow addition of drops of  $\text{Mn}^{2+}$  solution into the  $\text{CO}_3^{2-}$  solution, under open atmosphere and at ambient conditions, at controlled dropping and stirring rates ( $4 \text{ mL min}^{-1}$ , 400 rpm). The solution was then stirred for 1 h after the addition was completed. The precipitated powder was washed, centrifuged several times in DI  $\text{H}_2\text{O}$  and once with ethanol, and dried overnight at  $50^\circ\text{C}$  under vacuum.

ii) Hydrothermal (HT) method:<sup>[30,33]</sup> 50 mL of  $\text{CO}_3^{2-}$  solution was transferred to a beaker. An appropriate amount of an L-AA was added to the solution (the same amounts and concentrations and the same stirring procedure as described for the DD route). This was followed by the rapid addition of 50 mL of  $\text{Mn}^{2+}$  solution to the beaker, which was immediately transferred to a pre-heated autoclave. The autoclave was sealed and kept at  $134^\circ\text{C}$  ( $\approx 3$  bar) for 2 h, after which it was allowed to cool to room temperature. The resulting powder was washed and dried as for the DD method. In both synthesis routes, control samples with no added amino acids were also prepared.

Samples for the NPD experiments were prepared as described above, but because of the higher amounts of material needed for these experiments, four times the amounts of solution (i.e., 200 mL) was used in each case.

**Magnetization Measurements:** Magnetic measurements were carried out at the Quantum Matter Research (QMR) center in the Department of Physics at the Technion. A few mg of each MCO sample was loaded into a plastic holder, which was placed inside a brass tube. The tube was placed inside the SQUID magnetometer (MPMS3, Quantum Design) and the system was sealed and purged with helium. Each sample underwent two types of measurements: magnetic moment versus magnetic field ( $M-H$ ) at a constant temperature (300 and 2 K), and magnetic moment versus temperature ( $M-T$ ) at a constant magnetic field (10 Oe), while heating from 2 up to 75 K and after cooling to 2 K at zero magnetic field.

**Amino Acid Analysis (AAA):** As a first step, AAs were removed from crystal surfaces by the addition of 1 mL of 1 M NaOH solution to several milligrams of a sample within an Eppendorf tube. The tube was sealed and agitated for 30 s, and the samples were then centrifuged and washed twice with DI water and twice with acetone. AAA was performed in Xell AG (Bielefeld, Germany). Each sample was dissolved in a weak HCl solution, and this was followed by a derivatization process with AQC (6-aminoquinolyl-*N*-hydroxysuccinimidyl carbamate).<sup>[71,72]</sup> The samples were injected into an ultrahigh-performance liquid chromatograph (UHPLC, Agilent 1290) and AAs were detected using a UV (DAD detector).

**High-Resolution Powder X-Ray Diffraction:** HR-PXRD was carried out on beamline ID22 of the European Synchrotron Radiation Facility (ESRF) in Grenoble, France.<sup>[73]</sup> Several milligrams of each sample was transferred into borosilicate capillaries (0.5–0.7 mm in diameter), which were sealed using wax. The beam energy during the measurement was set at 35 keV. All samples were measured at room temperature, while selected samples were measured at 5 K, using liquid helium. Several samples were also measured after ex situ annealing treatment ( $200^\circ\text{C}$  for 4 h, under vacuum). Rietveld refinement was performed on each diffractogram using the GSAS-II software,<sup>[74]</sup> and the lattice parameters of each sample, as well as diffraction peak width parameters, were extracted.

**Neutron Powder Diffraction:** Room-temperature (300 K) and low-temperature (3 K) NPD experiments were undertaken on the KANDI-II powder diffractometer at the Israeli Research Reactor II (IRR-II) at the Nuclear Research Centre – Negev (NRCN).<sup>[75]</sup> A monochromatic beam with a wavelength of  $\lambda = 2.47(1)$  Å was obtained using the (002) reflection from a pyrolytic graphite monochromator. Powdered samples were loaded into vanadium cylindrical sample holders, each of

10 mm diameter and  $\approx 0.2$  mm wall thickness. Diffraction patterns were analyzed using Rietveld analysis,<sup>[76]</sup> employing the FULLPROF code.<sup>[77]</sup> Low temperature was achieved using a closed cycle helium refrigerator.

**Scanning Electron Microscopy:** HR-SEM images were obtained with a Zeiss Ultra+ high-resolution scanning electron microscope. The primary electron energy was set to 1.5 keV for all samples; hence, no conductive coating was needed.

## Supporting Information

Supporting Information is available from the Wiley Online Library or from the author.

## Acknowledgements

The authors thank Dr. Anna Eyal from the Quantum Matter Research (QMR) Center in the Physics Department, Technion, Haifa, for help with the magnetic measurements. Diffraction experiments were performed on beamline ID22 (experiment MA 4534) at the European Synchrotron Radiation Facility (ESRF), Grenoble, France. A.L. acknowledges financial support by the Israeli Ministry of Energy, as part of the scholarships program for M.Sc. and Ph.D. students.

## Conflict of Interest

The authors declare no conflict of interest.

## Data Availability Statement

The data that support the findings of this study are available from the corresponding author upon reasonable request.

## Keywords

amino acids, bioinspiration, Dzyaloshinskii–Moriya interaction, magnetic properties

Received: February 20, 2022

Revised: June 9, 2022

Published online: July 27, 2022

- [1] H. A. Lowenstam, S. Weiner, *On Biomineralization*, Oxford University Press, Oxford, UK **1989**.  
 [2] Y. Ma, S. R. Cohen, L. Addadi, S. Weiner, *Adv. Mater.* **2008**, *20*, 1555.  
 [3] M. H. Nesson, H. A. Lowenstam, **1985**, 333.  
 [4] E. Beniash, J. Aizenberg, L. Addadi, S. Weiner, *Proc. R. Soc. B* **1997**, *264*, 461.  
 [5] Y. Politi, T. Arad, E. Klein, S. Weiner, L. Addadi, *Science* **2004**, *306*, 1161.  
 [6] P. Fratzl, H. S. Gupta, E. P. Paschalis, P. Roschger, *J. Mater. Chem.* **2004**, *14*, 2115.  
 [7] H. Peterlik, P. Roschger, K. Klaushofer, P. Fratzl, *Nat. Mater.* **2006**, *5*, 52.  
 [8] J. Aizenberg, A. Tkachenko, S. Weiner, L. Addadi, G. Hendler, *Nature* **2001**, *412*, 819.  
 [9] R. Blakemore, *Science* **1975**, *190*, 377.  
 [10] C. Walcott, J. L. Gould, J. L. Kirschvink, *Science* **1979**, *205*, 1027.

- [11] P. P. Grassi-Schultheiss, F. Heller, J. Dobson, *BioMetals* **1997**, *10*, 351.  
 [12] J. L. Kirschvink, D. S. Jones, B. J. MacFadden, *Magnetite Biomineralization and Magnetoreception in Organisms: A New Biomagnetism*, Topics in Geobiology, Vol. 5, Springer, New York **1985**.  
 [13] J. C. Weaver, Q. Wang, A. Miserez, A. Tantuuccio, R. Stromberg, K. N. Bozhilov, P. Maxwell, R. Nay, S. T. Heier, E. DiMasi, D. Kisailus, *Mater. Today* **2010**, *13*, 42.  
 [14] A. Herman, L. Addadi, S. Weiner, *Nature* **1988**, *331*, 546.  
 [15] A. Berman, L. Addadi, A. Kvick, L. Leiserowitz, M. Nelson, S. Weiner, *Science* **1990**, *250*, 664.  
 [16] S. Younis, Y. Kauffmann, L. Bloch, E. Zolotoyabko, *Cryst. Growth Des.* **2012**, *12*, 4574.  
 [17] B. Pokroy, J. P. Quintana, E. N. Caspi, A. Berner, E. Zolotoyabko, *Nat. Mater.* **2004**, *3*, 900.  
 [18] E. Seknazi, B. Pokroy, *Adv. Mater.* **2018**, *30*, 1707263.  
 [19] E. Beniash, *WIREs Nanomed. Nanobiotechnol.* **2011**, *3*, 47.  
 [20] Y.-Y. Kim, M. Semsarilar, J. D. Carloni, K. R. Cho, A. N. Kulak, I. Polishchuk, C. T. Hendley, P. J. M. Smeets, L. A. Fielding, B. Pokroy, C. C. Tang, L. A. Estroff, S. P. Baker, S. P. Armes, F. C. Meldrum, *Adv. Funct. Mater.* **2016**, *26*, 1382.  
 [21] Y. Y. Kim, K. Ganesan, P. Yang, A. N. Kulak, S. Borukhin, S. Pechook, L. Ribeiro, R. Kröger, S. J. Eichhorn, S. P. Armes, B. Pokroy, F. C. Meldrum, *Nat. Mater.* **2011**, *10*, 890.  
 [22] L. A. Estroff, I. Cohen, *Nat. Mater.* **2011**, *10*, 810.  
 [23] H. Li, H. L. Xin, D. A. Müller, L. A. Estroff, *Science* **2009**, *326*, 1244.  
 [24] Y. Liu, W. Yuan, Y. Shi, X. Chen, Y. Wang, H. Chen, H. Li, *Angew. Chem., Int. Ed.* **2014**, *53*, 4127.  
 [25] H. Li, L. A. Estroff, *Adv. Mater.* **2009**, *21*, 470.  
 [26] B. Marzec, D. C. Green, M. A. Holden, A. S. Coté, J. Ihli, S. Khalid, A. Kulak, D. Walker, C. Tang, D. M. Duffy, Y. Y. Kim, F. C. Meldrum, *Angew. Chem., Int. Ed.* **2018**, *57*, 8623.  
 [27] G. Magnabosco, M. Di Giosia, I. Polishchuk, E. Weber, S. Fermani, A. Bottoni, F. Zerbetto, P. G. Pelicci, B. Pokroy, S. Rapino, G. Falini, M. Calvaresi, *Adv. Healthcare Mater.* **2015**, *4*, 1510.  
 [28] E. Weber, L. Bloch, C. Guth, A. N. Fitch, I. M. Weiss, B. Pokroy, *Chem. Mater.* **2014**, *26*, 4925.  
 [29] M. Różycka, I. Coronado, K. Brach, J. Olesiak-Bańska, M. Samoć, M. Zarębski, J. Dobrucki, M. Ptak, E. Weber, I. Polishchuk, B. Pokroy, J. Stolarski, A. Ozyhar, *Chem. - Eur. J.* **2019**, *25*, 12740.  
 [30] A. Lang, S. Mijowska, I. Polishchuk, S. Fermani, G. Falini, A. Katsman, F. Marin, B. Pokroy, *Chem. - Eur. J.* **2020**, *26*, 16860.  
 [31] S. Borukhin, L. Bloch, T. Radlauer, A. H. Hill, A. N. Fitch, B. Pokroy, *Adv. Funct. Mater.* **2012**, *22*, 4216.  
 [32] Y.-Y. Kim, J. D. Carloni, B. Demarchi, D. Sparks, D. G. Reid, M. E. Kunitake, C. C. Tang, M. J. Duer, C. L. Freeman, B. Pokroy, K. Penkman, J. H. Harding, L. A. Estroff, S. P. Baker, F. C. Meldrum, *Nat. Mater.* **2016**, *15*, 903.  
 [33] S. Mijowska, I. Polishchuk, A. Lang, E. Seknazi, C. Dejoie, S. Fermani, G. Falini, N. Demitri, M. Polentarutti, A. Katsman, B. Pokroy, *Chem. Mater.* **2020**, *32*, 4205.  
 [34] A. Brif, G. Ankonina, C. Drathen, B. Pokroy, *Adv. Mater.* **2014**, *26*, 477.  
 [35] A. Brif, L. Bloch, B. Pokroy, *CrystEngComm* **2014**, *16*, 3268.  
 [36] I. Polishchuk, N. Bianco-Stein, A. Lang, M. Kurashvili, M. Caspary Toroker, A. Katsman, J. Feldmann, B. Pokroy, *Adv. Funct. Mater.* **2020**, *30*, 1910405.  
 [37] A. Lang, I. Polishchuk, E. Seknazi, J. Feldmann, A. Katsman, B. Pokroy, *Adv. Funct. Mater.* **2020**, *30*, 2005136.  
 [38] M. A. H. Muhammed, M. Lamers, V. Baumann, P. Dey, A. J. Blanch, I. Polishchuk, X.-T. Kong, D. Levy, A. S. Urban, A. O. Govorov, B. Pokroy, J. Rodríguez-Fernández, J. Feldmann, *J. Phys. Chem. C* **2018**, *122*, 6348.  
 [39] E. N. Maslen, V. A. Streltsov, N. R. Streltsova, N. Ishizawa, *Acta Crystallogr., Sect. B: Struct. Sci., Cryst. Eng. Mater.* **1995**, *51*, 929.

- [40] A. Kosterov, T. Frederichs, T. von Döbeneck, *Phys. Earth Planet. Inter.* **2006**, *154*, 234.
- [41] I. Dzyaloshinsky, *J. Phys. Chem. Solids* **1958**, *4*, 241.
- [42] T. Moriya, *Phys. Rev.* **1960**, *120*, 91.
- [43] G. Beutier, S. P. Collins, O. V. Dimitrova, V. E. Dmitrienko, M. I. Katsnelson, Y. O. Kvashnin, A. I. Lichtenstein, V. V. Mazurenko, A. G. A. Nisbet, E. N. Ovchinnikova, D. Pincini, *Phys. Rev. Lett.* **2017**, *119*, 167201.
- [44] H. Thoma, V. Hutanu, H. Deng, V. E. Dmitrienko, P. J. Brown, A. Gukasov, G. Roth, M. Angst, *Phys. Rev. X* **2021**, *11*, 011060.
- [45] M. Karuppaiah, R. Akilan, P. Sakthivel, S. Asaithambi, R. Shankar, R. Yuvakkumar, Y. Hayakawa, G. Ravi, *J. Energy Storage* **2020**, *27*, 101138.
- [46] S. Wu, C. Liu, D. A. Dinh, K. S. Hui, K. N. Hui, J. M. Yun, K. H. Kim, *ACS Sustainable Chem. Eng.* **2019**, *7*, 9763.
- [47] P. V. Vardhan, M. B. Idris, V. Ramanathan, S. Devaraj, *ChemistrySelect* **2018**, *3*, 6775.
- [48] M. J. Aragón, B. León, C. Pérez Vicente, J. L. Tirado, *J. Power Sources* **2011**, *196*, 2863.
- [49] M. J. Aragón, C. Pérez-Vicente, J. L. Tirado, *Electrochem. Commun.* **2007**, *9*, 1744.
- [50] L. Wang, Y. Sun, S. Zeng, C. Cui, H. Li, S. Xu, H. Wang, *CrystEngComm* **2016**, *18*, 8072.
- [51] H. Takehara, R. Shimizugawa, T. Tokai, *US5749935A* **1998**.
- [52] Y. Jia, L. Yang, R. Feng, H. Ma, D. Fan, T. Yan, R. Feng, B. Du, Q. Wei, *ACS Appl. Mater. Interfaces* **2019**, *11*, 7157.
- [53] B. Venugopal, T. D. Luckey, *Metal Toxicity in Mammals*, Vol. 2, Plenum Press, New York **1978**, p. 409.
- [54] X. Zhu, H. Xiong, Q. Zhou, Z. Zhao, Y. Zhang, Y. Li, S. Wang, S. Shi, *ACS Appl. Mater. Interfaces* **2021**, *13*, 18462.
- [55] Y. Cheng, S. Zhang, N. Kang, J. Huang, X. Lv, K. Wen, S. Ye, Z. Chen, X. Zhou, L. Ren, *ACS Appl. Mater. Interfaces* **2017**, *9*, 19296.
- [56] C.-L. Chen, J. Qi, J. Tao, R. N. Zuckermann, J. J. DeYoreo, *Sci. Rep.* **2015**, *4*, 6266.
- [57] B. Pokroy, A. N. Fitch, F. Marin, M. Kapon, N. Adir, E. Zolotoyabko, *J. Struct. Biol.* **2006**, *155*, 96.
- [58] B. Pokroy, A. Fitch, E. Zolotoyabko, *Adv. Mater.* **2006**, *18*, 2363.
- [59] K. Page, C. E. White, E. G. Estell, R. B. Neder, A. Llobet, T. Proffen, *J. Appl. Crystallogr.* **2011**, *44*, 532.
- [60] A. S. Borovik-Romanov, M. P. Orlova, *Sov. Phys. JETP* **1957**, *4*, 531.
- [61] A. S. Borovik-Romanov, *J. Exp. Theor. Phys.* **1959**, *36*, 766.
- [62] P. J. Brown, J. B. Forsyth, *Proc. Phys. Soc.* **1967**, *92*, 125.
- [63] N. A. Spaldin, *Magnetic Materials: Fundamentals and Device Applications*, Cambridge University Press, Cambridge, UK **2010**.
- [64] L. L. Hench, J. K. West, *Principles of Electronic Ceramics*, Wiley, New York **1990**.
- [65] E. Zolotoyabko, E. N. Caspi, J. S. Fieramosca, R. B. Von Dreele, F. Marin, G. Mor, L. Addadi, S. Weiner, Y. Politi, *Cryst. Growth Des.* **2010**, *10*, 1207.
- [66] G. A. Samara, A. A. Giardini, *Phys. Rev.* **1969**, *186*, 577.
- [67] T. Shimizu, T. Matsumoto, A. Goto, T. V. Chandrasekhar Rao, K. Yoshimura, K. Kosuge, *Phys. Rev. B* **2003**, *68*, 224433.
- [68] K. Kikoin, V. Fleurov, *Phys. Rev. B* **2006**, *74*, 174407.
- [69] G. Magnabosco, I. Polishchuk, F. Palomba, E. Rampazzo, L. Prodi, J. Aizenberg, B. Pokroy, G. Falini, *Cryst. Growth Des.* **2019**, *19*, 4429.
- [70] A. N. Kulak, P. Yang, Y.-Y. Kim, S. P. Armes, F. C. Meldrum, *Chem. Commun.* **2014**, *50*, 67.
- [71] L. Bosch, A. Alegría, R. Farré, *J. Chromatogr. B* **2006**, *831*, 176.
- [72] S. A. Cohen, K. M. De Antonis, *J. Chromatogr. A* **1994**, *661*, 25.
- [73] A. Lang, L. Portal, I. Polishchuk, B. Pokroy, Investigating the Effect of Amino Acid Incorporation into the Crystal Lattice of Magnetite: From Structure to Magnetic Properties, *European Synchrotron Radiation Facility (ESRF)*, <https://doi.org/10.1515/ESRF-ES-472484700>.
- [74] B. H. Toby, R. B. Von Dreele, *J. Appl. Crystallogr.* **2013**, *46*, 544.
- [75] B. Anasori, J. Lu, O. Rivin, M. Dahlgvist, J. Halim, C. Voigt, J. Rosen, L. Hultman, M. W. Barsoum, E. N. Caspi, *Inorg. Chem.* **2019**, *58*, 1100.
- [76] H. M. Rietveld, *J. Appl. Crystallogr.* **1969**, *2*, 65.
- [77] J. Rodríguez-Carvajal, *Phys. B* **1993**, *192*, 55.